Combustion and Flame 229 (2021) 111383

Contents lists available at ScienceDirect

Combustion and Flame

journal homepage: www.elsevier.com/locate/combustflame

A modeling approach for soot formation in non-premixed flames with elevated stoichiometric mixture fraction

Phillip R. Johnson, Rajan K. Chakrabarty, Benjamin M. Kumfer*

Department of Energy, Environmental, and Chemical Engineering, Center for Aerosol Science and Engineering, Washington University, St. Louis, MO 63130, USA

ARTICLE INFO

Article history:
Received 12 October 2020
Revised 18 February 2021
Accepted 20 February 2021

Keywords:
Soot modeling
Oxygen enrichment
Oxy-combustion
Strained flames
Counterflow flame

ABSTRACT

Most soot formation models have been developed with particular applications in mind and as such, are valid only for the range of fuel-air combustion conditions representative of the target application. This limits the applicability and versatility of most models, especially for combustion processes wherein the stoichiometric mixture fraction, Z_{st}, could vary widely. A soot-producing flame could become non-sooting (blue) with an increase in Z_{st} even while maintaining constant flame temperature. This paper presents a novel modeling approach to account for the unique flame characteristics at elevated-Z_{st} environments and their effect on soot formation. This modeling approach is designed to capture both the formation and the reversible processes that occur on the fuel-side of a diffusion flame in a way which is robust, simple, and can be utilized in diverse applications. Additionally, a new semi-empirical model is developed for extending two widely-used models–Leung-Lindstedt and Moss-Brookes–both of which render inaccurate predictions under varying Z_{st} conditions. When applied to the counterflow flame system, the soot volume fraction profiles predicted by incorporation of our new and modified models agree well with experimental observations reported in the literature for low Z_{st}. Using this modeling approach also resulted in the prediction of blue (soot-free) limit condition in a non-premixed counterflow flame for the first time. We show that this result cannot be obtained by considering formation processes alone and that the performance of semi-empirical soot formation models can be dramatically improved when applied to higher-Z_{st} flames if the reversible nature of soot formation at high temperature is considered.

1. Introduction

Over the past several decades, tremendous progress has been made towards the development of detailed soot formation models, which involve large chemical reaction mechanisms and aerosol dynamics to accurately capture the complex processes of gas pyrolysis, particle inception, and surface growth [1–8]. There also remains a need for less complex, or semi-empirical, soot formation models such as those available in some commercial CFD software packages [9], so that accurate predictions of soot volume fraction (*svf*) can be quickly obtained with low computational cost when modeling complex, industrial combustion systems. While a useful semi-empirical soot model should be robust and applicable over a wide range of combustion conditions, such soot models historically have been developed using the insights of traditional experimental studies in fuel-air flames. These flames contain large fuel-rich zones that are conducive for study of the soot formation process.

In non-premixed flames with an aliphatic fuel, the soot formation process begins via fuel pyrolysis into acetylene (C_2H_2) and other intermediates. Then, aromatics such as benzene (A_1) can be formed through several possible pathways, with propargyl self-combination being significant [10]. Given sufficient species and temperature conditions conducive to soot formation, these aromatic species will grow and combine to form nascent particles through an inception process which is not yet completely understood, though recent work focusing on the role of resonance-stabilized radicals has shed new light [11]. Once particles are formed, the dominant mode of soot mass addition is through surface growth processes which include the C_2H_2-based HACA scheme as well as aromatic condensation. Consequently, in the context of semi-empirical models, soot formation has been described as a temperature-driven process which occurs whenever precursors species (fuel, acetylene, or aromatics) are available in sufficient concentrations. Such formulations indicate that the effect

---

* Corresponding author.
E-mail address: kumferb@wustl.edu (B.M. Kumfer).

https://doi.org/10.1016/j.combustflame.2021.02.029

Nomenclature

A_s	surface area (m^2)
$[C_nH_m]$	concentration of species $(kmol/m^3)$
d_p	particle diameter (m)
$f(S)$	surface area function
k	reaction rate constant
K	strain rate $(1/s)$
LL	Leung-Lindstedt model
LLR	Leung-Lindstedt model with added reversibility
MB	Moss-Brookes model
MBR	Moss-Brookes model with added reversibility
N_{AV}	Avogadro's number
psp	particle stagnation plane
svf	soot volume fraction
T	temperature (K)
T_A	Arrhenius temperature (K)
u	axial velocity (m/s)
W_i	molecular weight of species i $(kmol/kg)$
X_i	mole fraction of species i
Y_i	mass fraction of species i
$Y_{F,B}$	mass fraction of fuel, in a burning mixture
$Y_{F,U}$	mass fraction of fuel, in an unburning mixture
$Y_{O,U}$	mass fraction of oxidizer, in an unburning mixture
Z	mixture fraction
Z_{cr}	critical mixture fraction at which soot can being to form
Z_{ox}	oxidative mixture fraction at which soot can no longer form
Z_{st}	mixture fraction at stoichiometry
ν	stoichiometric quantity
ρ	gas mass density (kg/m^3)
ρ_S	soot particle mass density (kg/m^3)
φ	local equivalence ratio
Φ	normalized local equivalence ratio
ω_S	total soot formation rate $(kg/m^3 \cdot s)$
ω_{inc}	soot inception rate $(kg/m^3 \cdot s)$
ω_{SG}	soot surface growth rate $(kg/m^3 \cdot s)$
ω_{rev}	soot reversibility rate $(kg/m^3 \cdot s)$

of reduced soot formation upon increasing Z_{st} is solely due to fuel dilution. However, both fuel dilution and oxygen enrichment alter the basic structure of nonpremixed flames [10,12] and impact the stoichiometric mixture fraction, Z_{st}, Eq. (1).

$$Z_{st} = \left(1 + \frac{Y_{F,0}W_O\nu_O}{Y_{O,0}W_F\nu_F}\right)^{-1} \tag{1}$$

Soot formation is known to be strongly affected by Z_{st}. Flames can even transition from soot-producing (yellow) to non-sooting (blue) when Z_{st} is increased through the combination of oxygen enrichment and fuel dilution [13,14]. This result occurs even when the stoichiometric flame temperature is held constant and has been confirmed in a wide variety of non-premixed flame configurations including normal and inverted laminar coflow flames [15,16], turbulent jet flames [17], counterflow flames [18], and spherical flames produced in microgravity [19].

Previous work by this group has shown an inadequacy of existing one- and two-step semi-empirical models when applied to such elevated-Z_{st} and high-strain flames [20]. In general, existing models tend to over-predict soot formation for these conditions and were found to be unable to predict the experimentally measured yellow-to-blue transition at the soot inception limit. The current work will present a new modeling approach to account for the unique flame characteristics of elevated-Z_{st} environments and the effect on soot formation.

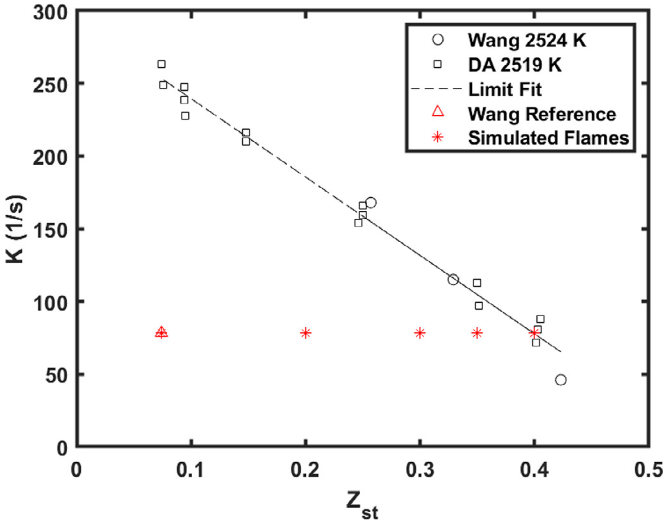

Fig. 1. Simulated flame conditions (red) and experimentally reported sooting limits for C_2H_4 combustion. (Wang et al. [22] in black circles, Du, Axelbaum (DA) [18] in black squares) in terms of K (velocity gradient upstream of the flame on the oxidizer side [25]) and Z_{st}. Soot forms for flames to the left of the limit (the flame is visibly "yellow") and does not form for flames to the right of the limit (the flame is visibly "blue"). The Wang Reference flame condition is from [23]. (For interpretation of the references to colour in this figure legend, the reader is referred to the web version of this article.)

2. Methods

The new approach to soot formation modeling is informed by analysis of a detailed chemical reaction mechanism and is evaluated in the counterflow flame system. Simulations of counterflow flames are performed using the CHEMKIN Pro [21] Opposed Flow module. The KM2 detailed combustion mechanism [2] is used to obtain the velocity, temperature and gas-phase species distributions. The CHEMKIN output data is post-processed in a MATLAB subroutine to solve the soot conservation equation(s) and calculate *svf*. Both this post-process subroutine and the use of KM2 have been previously justified by comparison with other modeling predictions in the literature [20].

As mentioned above, soot formation can be greatly affected in the counterflow flame and even eliminated, such that a blue flame is produced, by increasing Z_{st}. This phenonmenon has been demonstrated by the soot inception limits measured by Du and Axelbaum [18] and Wang et al. [22] and shown in Fig. 1. The region to the left of the limit line corresponds to flame conditions for which visible light emissions from soot particles could be observed; to the right of the limit the soot concentration is below the detection limits and appears blue. Figure 2 also indicates a series of simulated flame conditions that span the yellow-to-blue transition that are used to evaluate the soot models presented in this work. These flames are also listed in Table 1 along with two other experimental flame sets which are used for model validation. The $Z_{st} = 0.074$ flame matches that of Wang et al. [23], who measured *svf* profiles for these conditions. These measurements are used as a reference to normalize the semi-empirical models developed below. At $Z_{st} = 0.393$, the flame conditions are experimentally blue and the peak *svf* for this condition is considered to be less than 0.01 ppm (the diagnostic detection limit). More information can be found in our previous work using this methodology [20].

Previous work has also shown that it is beneficial to analyze soot formation rate by plotting as a function of the normalized

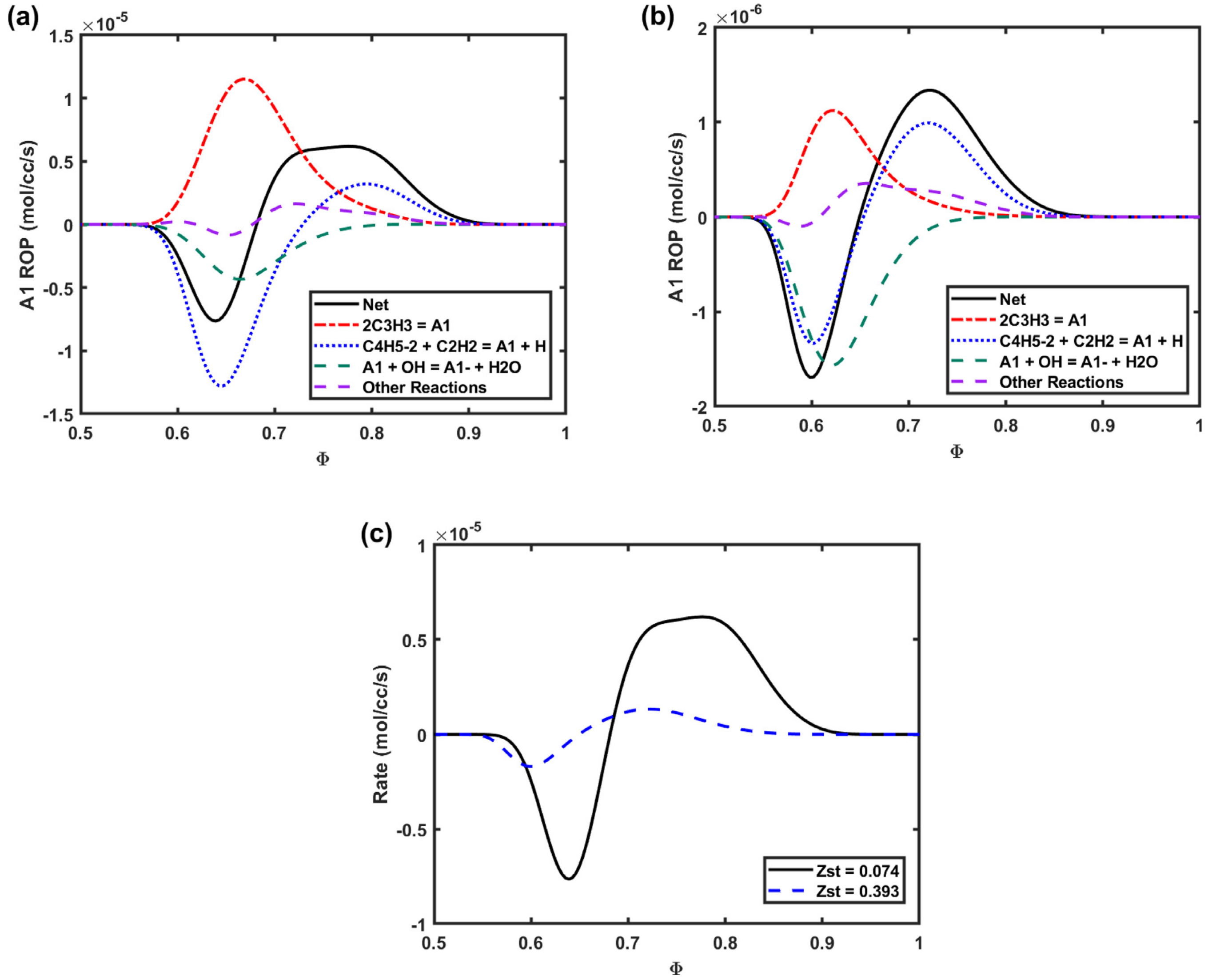

Fig. 2. A_1 Rate of Production vs Φ. a) Various pathways for $Z_{st} = 0.074$, b) Various pathways for $Z_{st} = 0.393$, c) Comparison of net A_1 ROP against $Z_{st} = 0.074$ and 0.393. (For interpretation of the references to colour in this figure legend, the reader is referred to the web version of this article.)

Table 1
List of flame conditions for simulations. $Y_{F,0}$ is the mass fraction in the fuel inlet. $Y_{O2,0}$ is the oxygen fraction in the oxidizer inlet, Z_{st} is the stoichiometric mixture fraction, T_{AD} is the adiabatic flame temperature (K), T_{Peak} is the actual max temperature (K) from the simulated flame, U_0 is the inlet velocity (cm/s), D is the distance (cm) between jets. For all flames in this study, the fuel species used was C_2H_4. When simulating experimental flames from the literature, a citation has been given.

Flame Name, Source	$Y_{F,0}$	$Y_{O2,0}$	Z_{st}	T_{AD}	T_{Peak}	U_0	D
$Z_{st} = 0.074$ [23]	1.0	0.276	0.074	2517	2285	30	0.8
$Z_{st} = 0.196$	0.380	0.318	0.196	2517	2251	30	0.8
$Z_{st} = 0.291$	0.256	0.360	0.291	2517	2224	30	0.8
$Z_{st} = 0.347$	0.215	0.391	0.347	2517	2213	30	0.8
$Z_{st} = 0.393$	0.190	0.422	0.393	2517	2210	30	0.8
Hwang SF 20 [14]	1.0	0.222	0.055	2322	2056	19.5	1.42
Xu SF 30 [24]	1.0	0.329	0.088	2649	2490	20	0.8

local equivalence ratio, (Φ) [20]. The local equivalence ratio (φ), can be calculated numerous ways, as in Eq. (2). A normalized Φ is used in this study to obtain a finite range of values (Eq. (3)). The location of stoichiometry does not change with flame conditions or with fuel species, being always located at $\varphi = 1$, ($\Phi = 0.5$).

$$\varphi = \nu \frac{Y_{F,U}}{Y_{O,U}} = \left(\frac{Z}{1-Z}\right)\left(\frac{1-Z_{st}}{Z_{st}}\right) = \frac{m_C + m_H/m_O}{(m_C + m_H/m_O)_{st}} \tag{2}$$

$$\Phi = \frac{\varphi}{\varphi + 1} \tag{3}$$

3. Theory and model development

3.1. Soot precursor chemistry

The goal of the semi-empirical model formulations produced in this work is to capture important chemical phenomena during soot formation in the most concise and accurate manner as possible. It is helpful to recall important chemical pathways which are relevant in the flame environments of interest. Soot formation is often thought to proceed everywhere on the fuel-side of the non-premixed flame, until the pool of oxidative species (e.g. O_2, OH) is reached, as evidenced by the formulation of existing semi-empirical models. However, other processes counteract soot formation which occur in all flames and become more pronounced, even critical, at elevated Z_{st}. Previous studies have indicated that soot stops forming prior to reaching the location of oxidizing species, due to various reversibilities in the soot formation process. Temperature can affect soot reversibility due to the exothermic nature of the C_2H_2-to-A1 pathway [1] and can also play a role in PAH fragmentation [1]. Elvati and Violi [26] have shown that PAH dimers are thermodynamically unstable at high temperatures. Accounting for reversibility in aromatic condensation has also been shown to be important for predicting particle morphology [27].

Significant work has been done on the role of soot precursor chemistry, whether precursor consumption [28] or the reversal of pathways leading to aromatic ring formation [1,29]. Skeen, et al. [10] examined the effect of Z_{st} on chemical reaction pathways critical to soot inception by modeling a series of counterflow flames with the USC-II mechanism. Propargyl self-combination was seen as the dominant pathway for aromatic ring formation and the authors concluded that this formation reaction reverses at high Z_{st} due to an increase in the H atom concentration. Skeen et al. analyzed several potential pathways to aromatic formation, two of which are shown in Eqs. (4)-(5). They argued that Eq. (4) should be given precedence over Eq. (5) because its integrated contribution was seven times larger and that Eq. (4) was affected by Z_{st}-based flame structure effects while Eq. (5) was pyrolysis-based and controlled by dilution. They also noted that Eq. (4) is endothermic, being predominant at higher temperatures (>1600 K) before reaching the H pool while Eq. (5) is exothermic and favored and lower temperatures (<1600 K)

$$2C_3H_3 = A_1^- + H \tag{4}$$

$$C_4H_5 + C_2H_2 = A_1 + H \tag{5}$$

These features can be observed in Fig. 2, which shows the pathways of A_1 formation for $Z_{st} = 0.074$ (Fig. 2a) and for the soot inception limit flame ($Z_{st} = 0.393$, Fig. 2b). While Eq. (4) is still more productive than Eq. (5) in terms of peak and integrated rate, these metrics mask the local importance of each reaction. In the region where Eq. (5) has reversed ($0.6 < \Phi < 0.7$), it is counteracting Eq. (4). Moving from the fuel inlet to the flame (right to left in Fig. 2), the main contribution to A_1 generation is initially due to Eq. (5), then a mix of Eqs. (4)-(5), then Eq. (4), and finally the net reaction flips and A_1 is destroyed due to a combination of Eq. (5), oxidation from OH, and other contributions. Note that in the location where Eq. (4) peaks, the net A_1 ROP is actually negative due to the factors of reversibility and oxidation. The overall result of these effects is that the net A_1 ROP more closely follows Eq. (5) in its profile shape and reverses in the high temperature zone. For $Z_{st} = 0.393$, these features are similar with the notable observation that all rates are reduced. Fig. 2c shows the A_1 ROP comparison for these two flames. For $Z_{st} = 0.074$, the reversal happens around $\Phi = 0.68$ and for $Z_{st} = 0.393$, $\Phi = 0.65$. Given that Eq. (5) reverses with the H atom pool, these arguments further promote the overall argument of Skeen et al., that hydrogen is an important contributor in the reversal of soot-promoting pathways. The novelty of these observations is the emphasis on the *locality* ($\Phi \sim 0.65$) at which this occurs for all Z_{st}.

Skeen et al. also hypothesized that these behaviors would be observed for other soot precursor growth reactions where hydrogen is generated as a product, e.g. there would be a reduction in PAH growth due to this set of reactions. To investigate this claim, an analysis was performed on all carbon addition reactions from A_1 up to A_7 in the KM2 mechanism. Examples of these types of reactions involving acetylene are shown in Eqs. (6)–8 below.

$$A_1^- + C_2H_2 \leftrightarrow A_1C_2H + H \tag{6}$$

$$A_2 + C_2H_2 \leftrightarrow A_2C_2H_2 \tag{7}$$

$$A_2C_2H + C_2H_2 \rightarrow A_3 \tag{8}$$

Table 2
Critical C/O values below which no soot can form as measured by Kumfer et al. [30], followed by the C/O of stoichiometry for each fuel, and the critical values converted to φ and Φ.

Fuel	Measured critical C/O [30]	Stoichiometric C/O	φ_{cr}	Φ_{cr}
CH_4	0.42	0.25	1.68	0.63
C_2H_6	0.54	0.29	1.89	0.65
C_3H_8	0.58	0.30	1.93	0.66
C_2H_4	0.60	0.33	1.80	0.64
C_2H_2	0.71	0.40	1.78	0.64

Other important carbon-addition reactions, many of which are reversible, are listed in the Supplemental Material. These carbon-reactions are summed together and plotted in Fig. 3a, for both low-and high-Z_{st} flames. The various carbon-adding reactions are grouped according to their by-products: reactions with no by-product (Eq. (8)), reactions with a by-product of H (Eq. (6)), and reactions with a by-product of H_2 (Eq. (7)). These three reaction groupings are plotted separately for $Z_{st} = 0.074$ in Fig. 3b. A complete list of reactions used is included in the supplemental material. For the flame condition of $Z_{st} = 0.74$, at the location near $\Phi = 0.65$ there is a reversal in the net chemical rate where the reactions are no longer favorable for carbon addition; rather, reverse reactions are promoted which remove attached carbon species. For the soot inception limit flame ($Z_{st} = 0.393$), the transition occurs closer to $\Phi = 0.60$ but the trend is similar (notably, the positive quantity of carbon addition is also reduced due the diminished formation of precursors, e.g. A_1 as noted by Skeen et al. [10]). Figure 3b indicates that while there are multiple reaction types which contribute to net carbon addition, the reversal effect is solely due to reactions where a by-product of H atom is produced. This result is consistent with the H-based reversal of Eqs. (4)–5 above and collectively, these reactions demonstrate that H-based reversals occur at all levels of soot formation (C_3H_3 formation, aromatic creation, PAH growth) and that the reversibility of soot formation occurs in the region of $0.60 < \Phi < 0.70$.

These results are consistent with the findings of Kumfer, et al. [30] concerning an observed high-temperature boundary of the soot-formation zone away from flame front where soot could no longer form. In that work, this location can be characterized by a critical local equivalence C/O ratio [30] for several different aliphatic fuels in a non-premixed coflow flame. For ethylene, $C/O|_{cr}$ was determined to be 0.53 [30], which is relatively far from the location of stoichiometry ($C/O = 0.33$). By converting the various C/O ratios to Φ, this boundary can be referred to generally. As seen in Table 2, the critical value(s) take a very narrow range (0.63–0.66) upon conversion from C/O to Φ, as the latter is applicable to all fuel species. Beyond this location the local gas composition and/or temperature are not favorable for soot inception. It is now hypothesized that there is a balance in the formation and reversing processes at this location such that there is no net soot formation beyond this location for all flame conditions. As Z_{st} increases, the soot formation zone shrinks in size until the location of initial soot formation coincides with this critical location [15].

Given the observed importance of these reversible reactions and the role that hydrogen plays in this process, it would be beneficial to capture these features in a semi-empirical soot model. As with previous work, the target will be semi-empirical models due to an application focus and desire to capture important chemical details in a simple manner. The latter point is non-trivial as the ability to concisely describe physical phenomenon coincides with elucidating important features. In brief, a new reversibility term is proposed for use in semi-empirical soot modeling. Because modeling of reactions involving the H atom would require an extensive mechanism, instead a temperature-based reversibility term is

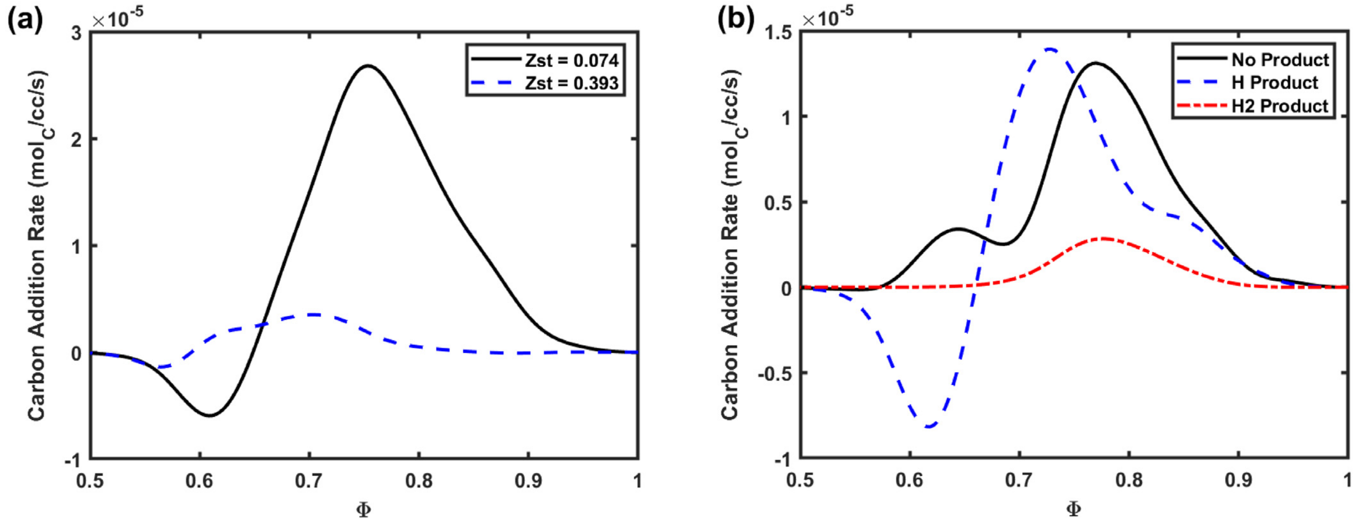

Fig. 3. Analysis of carbon-addition pathways from A_1 to A_7 for the KM2 mechanism. a) All reactions summed for $Z_{st} = 0.074$ and $Z_{st} = 0.393$. b) Reactions grouped and summed according to reaction by-product for $Z_{st} = 0.074$.

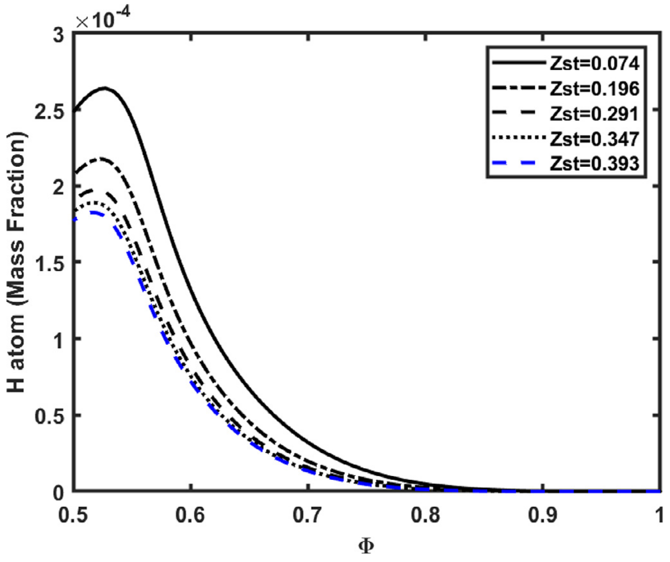

Fig. 4. Hydrogen atom fraction vs. Φ as predicted by KM2 for various Z_{st}. (For interpretation of the references to colour in this figure legend, the reader is referred to the web version of this article.)

added which serves as a proxy for a hydrogen-based reactions that counteract soot formation. This analogy is shown in Eq. (9) below.

$$\omega_{rev} = k_{rev} \exp\left(-\frac{T_{A,rev}}{T}\right) \sim \; k_H[H] \tag{9}$$

High temperature can be a good indicator of the location of H atom, as seen in Fig. 4 where the peak of H is located somewhat close to the flame (but on the fuel side) and quickly declines as temperature drops. An additional reason for basing the reversibility term below (Eq. (12)) on temperature is the various temperature-based reversibilities hindering soot inception described above. Capturing these features, while less critical for traditional fuel-air flames, is essential for high-Z_{st} environments where these processes can suppress and even inhibit soot formation.

3.2. Model formulation

Given these various considerations, we propose an alternative semi-empirical modeling approach with the aim to capture the competition between formation and the reversing processes that occur on the fuel-side of a diffusion flame. This two-term formulation indicates competition between these processes, with the total soot formation being the net sum between the two. For this new model, the net soot production is zero at the location $\Phi = 0.65$, indicating that the soot-formation process is balanced by reversibility. This value was chosen as the median value of the reversibility region as observed in Figs. 3, 4 and was in the bounds of Φ as determined by Table 2. It is recognized that to fully capture the nuances of this phenomenon would require modeling at a level of detail is beyond the aim and scope of this work, which is to capture this effect conceptually and concisely. This effect is achieved by fitting the various rate constants so that the overall rate becomes zero at this location, as described further below.

Formation-Reversible Model:

$$\omega_S = \omega_{form} - \omega_{rev} \tag{10}$$

$$\omega_{form} = k_{form} \rho Y_{F,B} \exp\left(-\frac{T_{A,form}}{T}\right) \tag{11}$$

$$\omega_{rev} = k_{rev} \exp\left(-\frac{T_{A,rev}}{T}\right) \tag{12}$$

where

$$Y_{F,B} = Y_{F,0} \frac{Z - Z_{st}}{1 - Z_{st}} \tag{13}$$

The formation Arrhenius temperature for a one-step soot formation process is set to $T_{A,form} = 15,600\ K$, as determined from measurements found the literature [31]. The leading constants for the two terms in the model and the activation temperature in Eq. (12) are determined by fitting to experimental data available in the literature and by using the procedure outlined below. In solving for the constants, three criteria are imposed: 1) that the resulting peak *svf* matches that of an experimental measurement for a particular reference flame condition [23] which is described below, 2) that no soot forms ($\omega_S = 0$) for $\Phi \leq 0.65$ in a soot inception limit flame (i.e., the formation and reversibility are equivalent

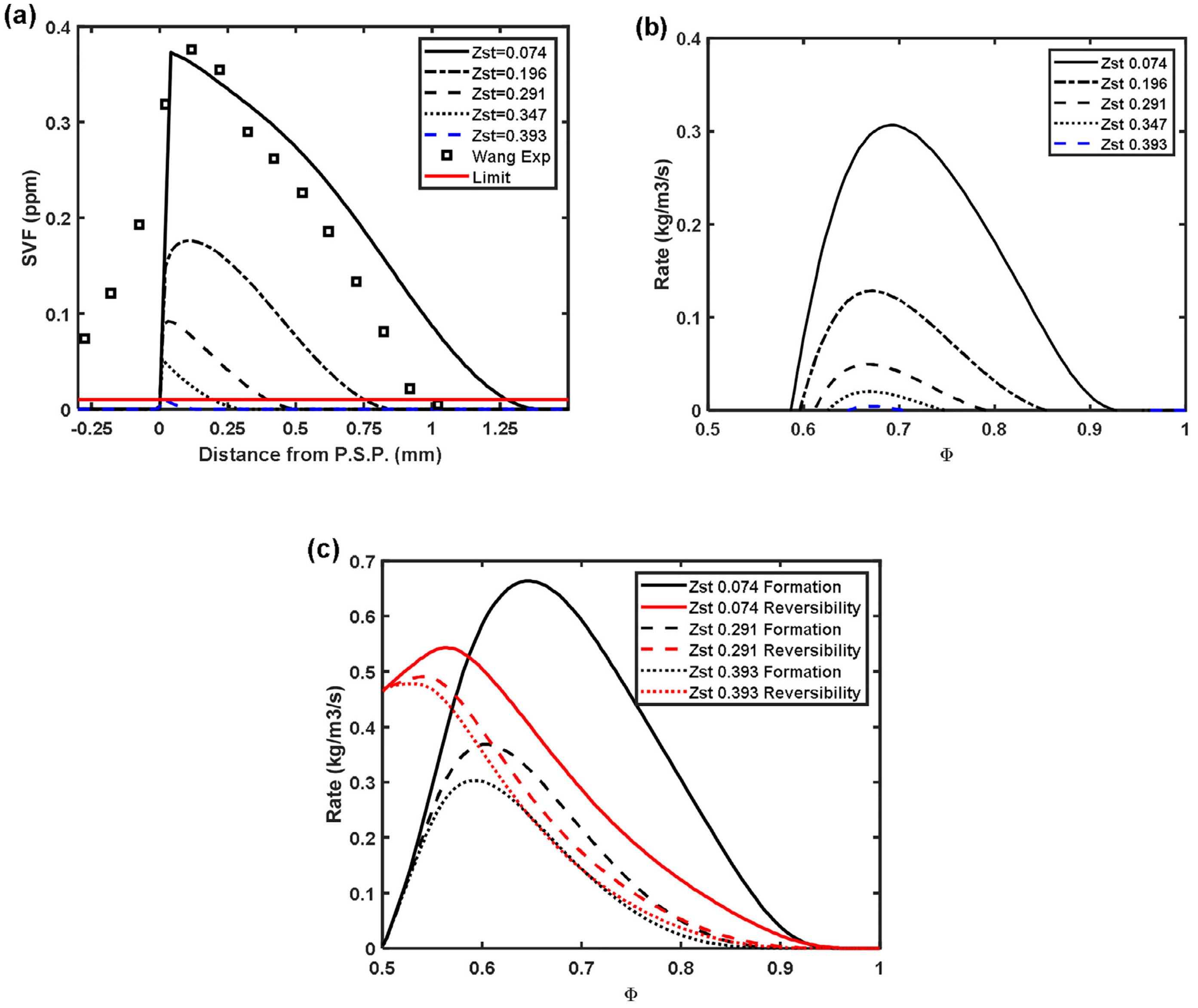

Fig. 5. Results from the new model for all Z_{st} in the changing Z_{st} evaluation; a) predicted and experimentally measured *svf* vs. distance from *psp*; diagnostic limit for *svf* shown by red line. b) total formation rate vs. Φ; c) formation and reversibility rates vs. Φ for 3 different Z_{st}. (For interpretation of the references to colour in this figure legend, the reader is referred to the web version of this article.)

at this location), and 3) that the model predicts a blue (soot-free) flame for the soot inception limit flame of the same strain (see Methods for quantification of this value). With these three conditions, the three remaining unknowns of Eqs. (11)–(12) (k_{form}, k_{rev}, $T_{A,rev}$) can be found. For the second and third conditions, the flame corresponding to $Z_{st} = 0.393$ (see Table 1 and Fig. 1) is the soot inception limit flame used for model validation. Eqs. (10)-(12) are iteratively solved to achieve a solution.

4. Results and discussion

4.1. One-step modeling results

The modeling constraints were satisfied with k_{form} = 1.19E5, k_{rev} = 22.4, $T_{\mathrm{A,rev}}$ = 8500 K and the results are shown in Fig. 5. Predictions of *svf* are shown in Fig. 5a; soot forms and is transported via convection (designated by arrows) to the particle stagnation plane (*psp*) where it accumulates, leading to the signature *svf* profile of the counterflow flame. The new model agrees well with the measured *svf* values at $Z_{\mathrm{st}} = 0.074$ [23], which can be directly verified by comparison with the experimental data points in Fig. 5a. The model also predicts the experimentally observed soot-free (blue) conditions for $Z_{\mathrm{st}} = 0.393$, as the peak *svf* is below the limit line where *svf* = 0.01 ppm.

The predicted soot formation rate profile is shown in Fig. 5b. Model results indicate that soot can form in a region between two boundaries as discussed in the theory section. Near the fuel inlet, soot begins to form (Φ ~ 0.92 for $Z_{\mathrm{st}} = 0.074$) as sufficient temperature is reached for the given fuel availability. On the high temperature side of the soot formation zone (Φ ~ 0.58 for $Z_{\mathrm{st}} = 0.074$), net soot production ceases as the reversing reactions surpass formation reactions. The region between this location and the flame front is not conducive to soot formation. As Z_{st} increases, the soot formation zone shrinks from both the right (high-Φ) and left (low-Φ) side of the zone. The model predicts a reduction of soot formation at higher-Φ due to the effect of dilution diminishes the fuel available to form soot. The model also predicts a reduction of soot formation at lower-Φ due to the effects captured by the reversibil-

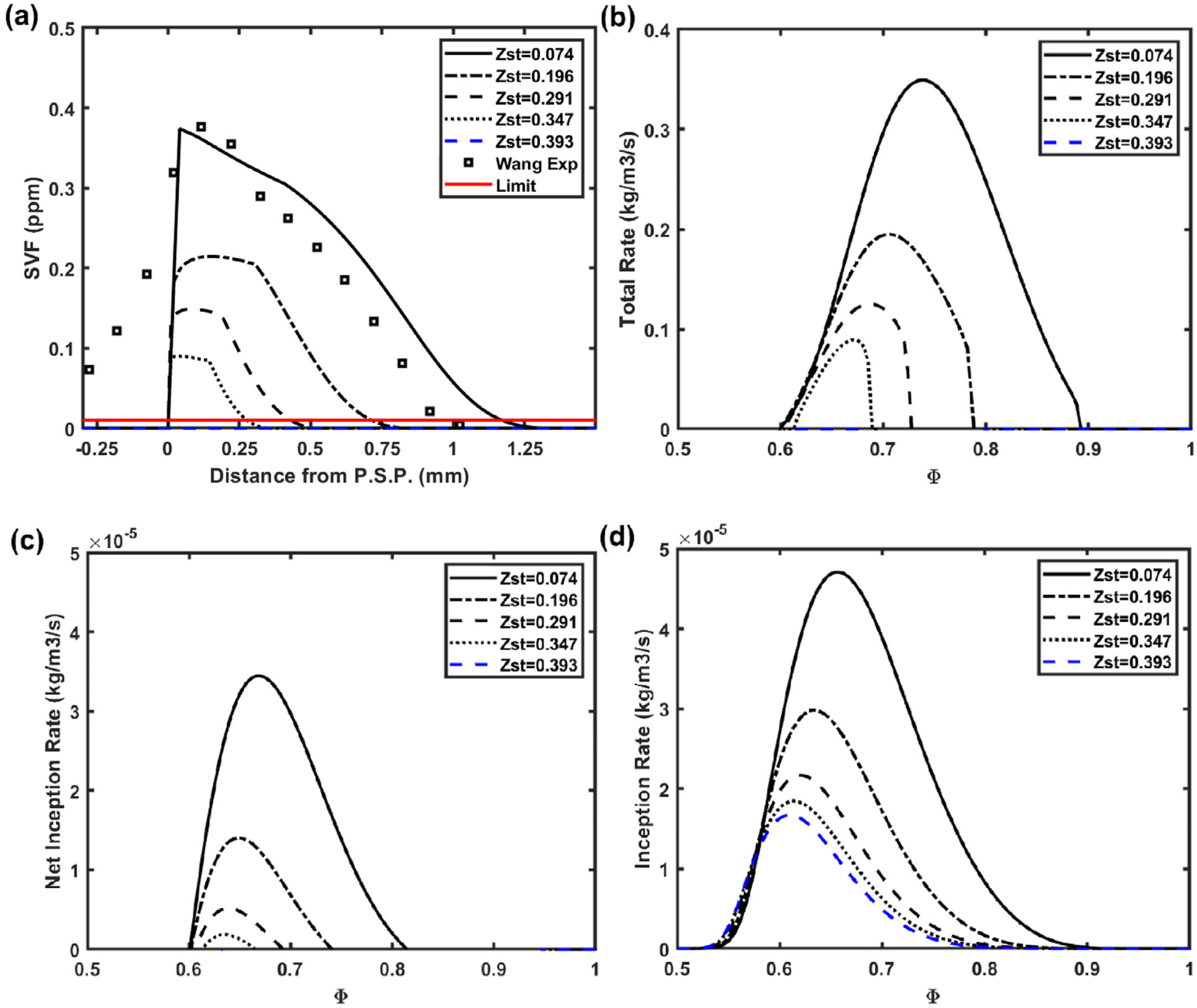

Fig. 6. Results from the Leung-Lindstedt-Reversible model for the changing Z_{st} evalulation; a) predicted and experimentally measured *svf* vs. distance from *psp*; diagnostic limit for *svf* shown by red line. Arrows indicate direction of gas convection. b) total formation rate vs. Φ; c) net inception $(\omega_{inc} - \omega_{rev})$ rate vs. Φ; d) inception rate (ω_{inc}) vs. Φ. (For interpretation of the references to colour in this figure legend, the reader is referred to the web version of this article.)

ity term (Eq. (12)). There are no direct experimental comparisons to the three intermediates Z_{st} (0.196, 0.291, 0.347) flames, which are displayed in Fig. 5 to indicate the gradual and continuous reduction of soot formation. Finally, at $Z_{st} = 0.393$, these reductions coincide to yield zero net soot formation. For this flame condition, no soot can form at Φ lower than the critical value, thus satisfying the third modeling constraint. This suppression of soot formation can also be seen by viewing the different formation (Eq. (11)) and reversibility (Eq. (12)) rates, as shown in Fig. 5c for $Z_{st} = 0.074$, 0.291, and 0.393. For $Z_{st} = 0.074$, there is a region where the formation rate is significantly higher than the reversibility rate. As Z_{st} increases, this gap narrows until at $Z_{st} = 0.393$, when reversibility has overtaken the formation rate everywhere.

Finally, the reversibility term in Fig. 5c can be compared to the mass fraction of H atom predicted by the detailed KM2 model for varying Z_{st} in Fig. 4. It is apparent that these two curves are similar in their shape, peak location, and their trend with Z_{st}. Therefore, it is with great interest that we note that the fitting parameters and therefore the shape of the reversibility curve were determined solely by the criteria of zeroing below Φ_{cr} and balancing the limit value at high Z_{st}. While it is recognized that the reversibility process is multi-faceted, this approach appears to capture the main feature. As a final note, the reversibility processes described in this paper are more focused on precursor chemistry and therefore could be seen to more directly affect the soot inception process rather than all soot formation. The following section will use this model framework to reverse the inception process only.

4.2. Semi-empirical models with reversibility

Since the formation-reversible model (Eq. 10) showed considerable successes at elevated Z_{st}, another layer of detail and potential accuracy was investigated where inception and surface growth are separately considered. Rather than develop new models, two established two-step semi-empirical models were used: the

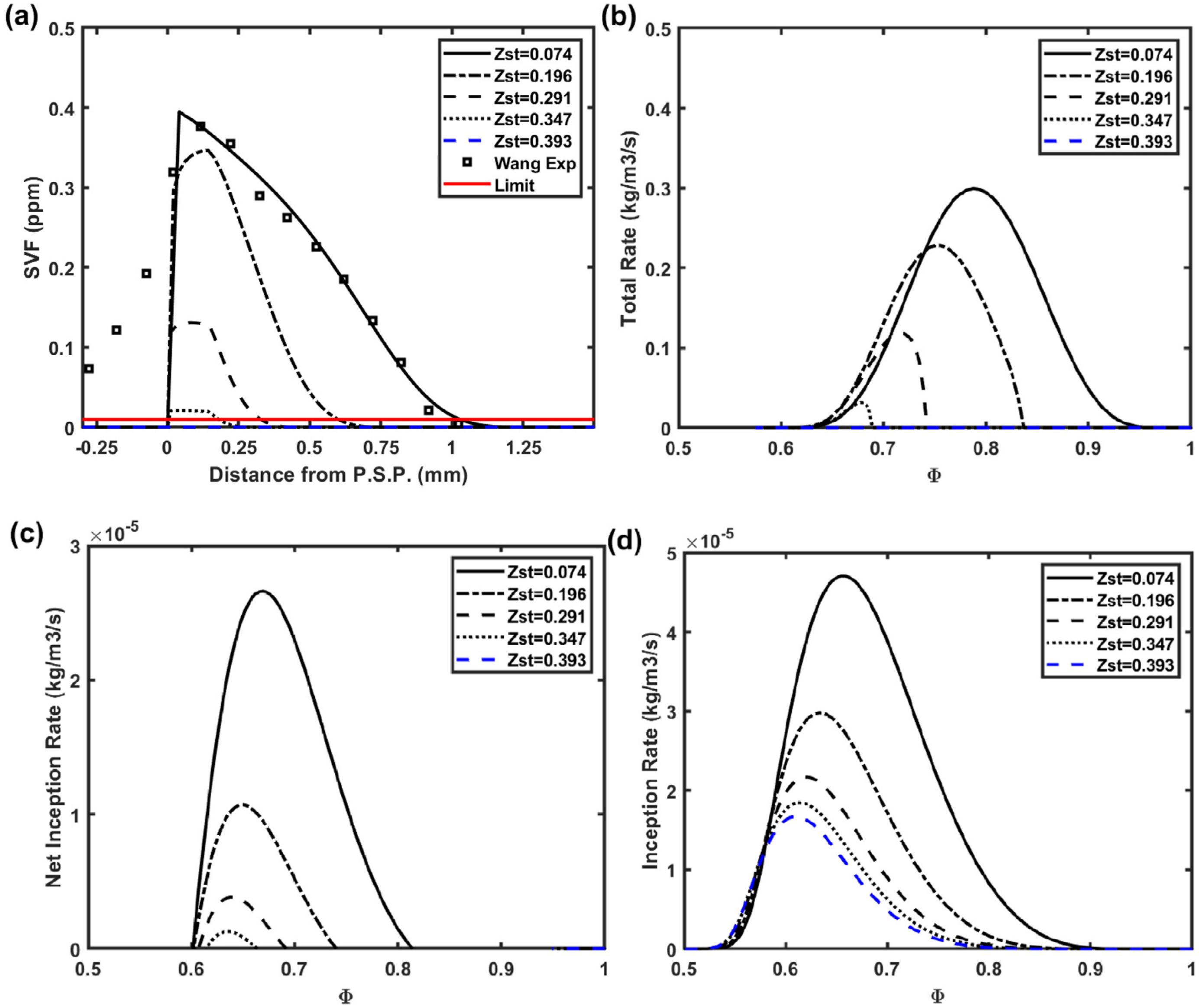

Fig. 7. Results from the Moss-Brookes-Reversible model for the changing Z_{st} evalulation; a) predicted and experimentally measured *svf* vs. distance from *psp*; diagnostic limit for *svf* shown by red line. Arrows indicate direction of gas convection. b) total formation rate vs. Φ; c) net inception ($\omega_{inc} - \omega_{rev}$) rate vs. Φ; d) inception rate vs. Φ. (For interpretation of the references to colour in this figure legend, the reader is referred to the web version of this article.)

Leung-Lindstedt (LL) model [32] and the Moss-Brookes (MB) model [33]. These two were chosen based on their popularity and because they show similarity of form but with varying fitting constants that result in different results for the same flame conditions (e.g. see results in [20]). Previous work by this group has shown their inadequacy at elevated Z_{st}, making them fitting candidates to investigate a reversibility-based remedy. The modified equations are shown below with terms from the original models (Eqs. (15)–(21)) included. The reversible forms of the models are labelled LLR and MBR, respectively.

Semi-Empirical Models, with Modification:

$$\omega_S = k_{norm}((\omega_{inc} - \omega_{rev}) + \omega_{sg}) \tag{13}$$

$$\omega_n = k_{norm}\left(\frac{N_{AV}}{M_P}\ (\omega_{inc} - \omega_{rev})\right) - \omega_{coag} \tag{14}$$

Leung-Lindstedt

$$\omega_{inc} = 10^4\ [C_2H_2]\ \exp\left(-\frac{21,100}{T}\right) \tag{15}$$

$$\omega_{sg} = f(S)\left(6 \times 10^3\right)\ [C_2H_2]\exp\left(-\frac{12,100}{T}\right) \tag{16}$$

$$f(S) = (A_s)^{0.5} = \left(\pi d_p^2 \rho n\right)^{0.5} = \left(\pi\left(\frac{6}{\pi}\frac{1}{\rho_S}\frac{Y_S}{n}\right)^{\frac{2}{3}}\ \rho n\right)^{0.5} \tag{17}$$

Moss-Brookes

$$\omega_{inc} = 7.78 \times 10^3[C_2H_2]\exp\left(-\frac{21,100}{T}\right) \tag{18}$$

$$\omega_{sg} = f(S)30.7[C_2H_2]^{0.4}\exp\left(-\frac{12,100}{T}\right) \tag{19}$$

$$S = A_s = \pi d_p^2 \rho n = \left(\pi\left(\frac{6}{\pi}\frac{1}{\rho_S}\frac{Y_S}{n}\right)^{\frac{2}{3}}\ \rho n\right)^1 \tag{20}$$

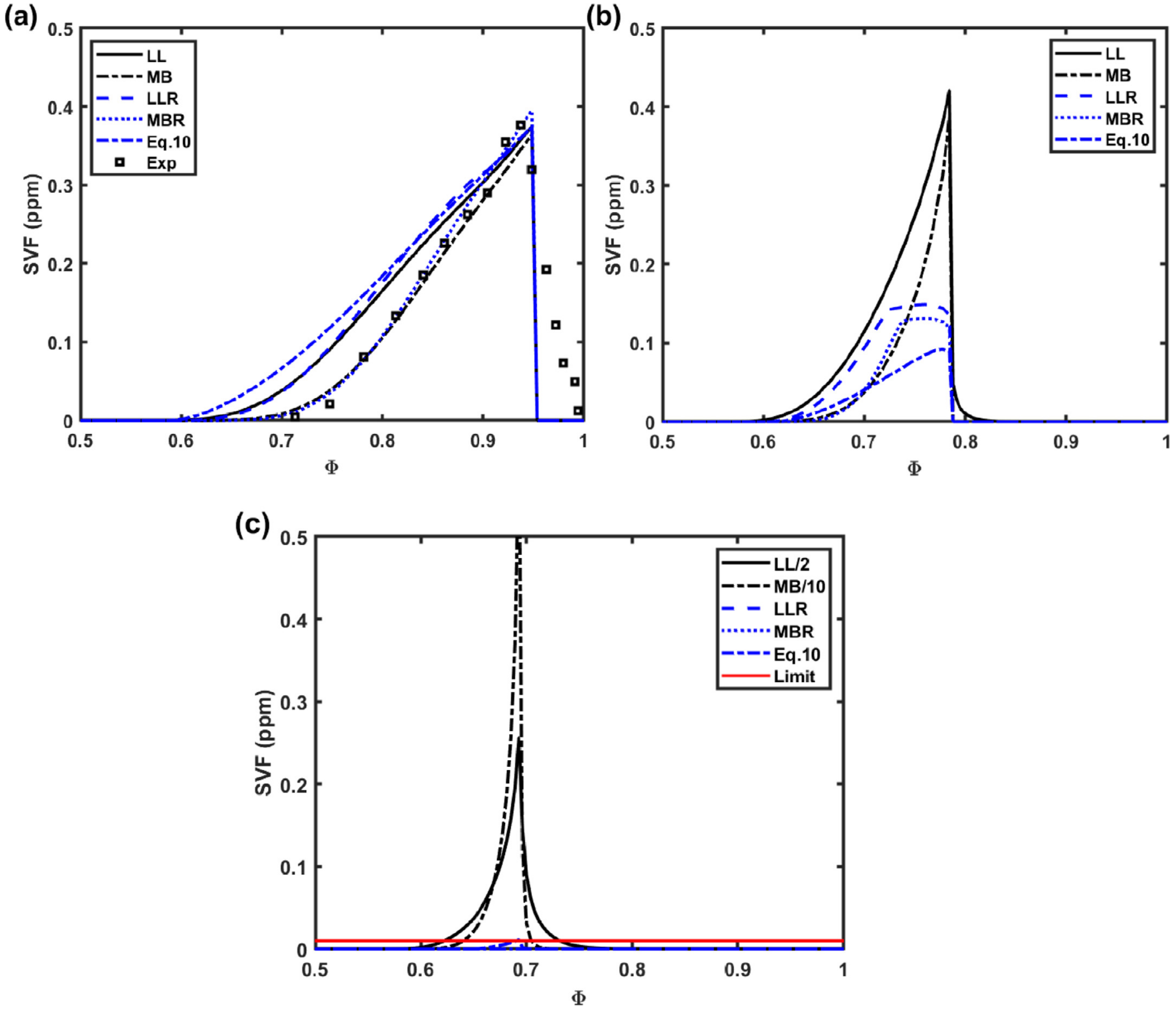

Fig. 8. Predicted *svf* vs Φ. for all models. a) $Z_{st} = 0.074$ (includes experimentally measured *svf* and diagnostic limit for *svf* shown by red line); b) $Z_{st} = 0.291$; c) $Z_{st} = 0.393$. (For interpretation of the references to colour in this figure legend, the reader is referred to the web version of this article.)

Semi-Empirical Reversible Terms

$$\omega_{rev,LL} = k_{rev}\exp\left(-\frac{T_{A,rev}}{T}\right) \tag{21}$$

$$\omega_{rev,MB} = k_{rev}\exp\left(-\frac{T_{A,rev}}{T}\right) \tag{22}$$

The value of $T_{A,rev}$ is retained as used in the formation-reversible model above (8500 K). However, since the reversibility term is only applicable to inception rather than total soot formation as in the former model, k_{rev} must be found by a different condition for these models. Similar to condition (2) above, here the condition is that no soot forms at $\Phi \leq 0.65$ at the soot inception limit ($Z_{st} = 0.393$, see Methods section); the *inception* and reversibility are now equivalent at this location. Finally, there is a normalization factor imposed on these semi-empirical models to adjust them such that the peak *svf* match that of an experimental measurement for a particular reference flame condition [23] which is described below, as in condition (1) above, and described previously for semi-empirical models [20]. The normalization factor is multiplied on the net inception ($\omega_{inc} - \omega_{rev}$) and mass surface growth (ω_{sg}) terms (see Eqs. (13)-(14)). The values of these constants are k_{norm}= 1.39, k_{rev} = 1.6E-3 (LLR) and k_{norm}= 4.8, k_{rev} = 1.2E-3 (MBR).

Results for the LLR model are shown in Fig. 6. The *svf* profiles, seen in Fig. 6a, show a steady decrease in peak *svf* as Z_{st} increases. At $Z_{st} = 0.074$, the peak value matches the experimental *svf*. For the experimental blue flame, the predicted peak is below the limit, thus correctly predicing soot-free conditions. In Fig. 6b, the predicted soot formation rate is shown. The rate is always bounded between $0.6 < \Phi < 0.9$. As Z_{st} increases, the zone region shrinks and the formation rate decreases. As the blue condition is approached, the peak formation rate location shifts to $\Phi = 0.65$. This result is consistent with the experimental observation as described above for the Φ_{cr} boundary. In Fig. 6c, the net nucleation rate for LLR is shown. Similar to the toal formation rate, there is steady decrease of the inception rate magnitude and the zone size also

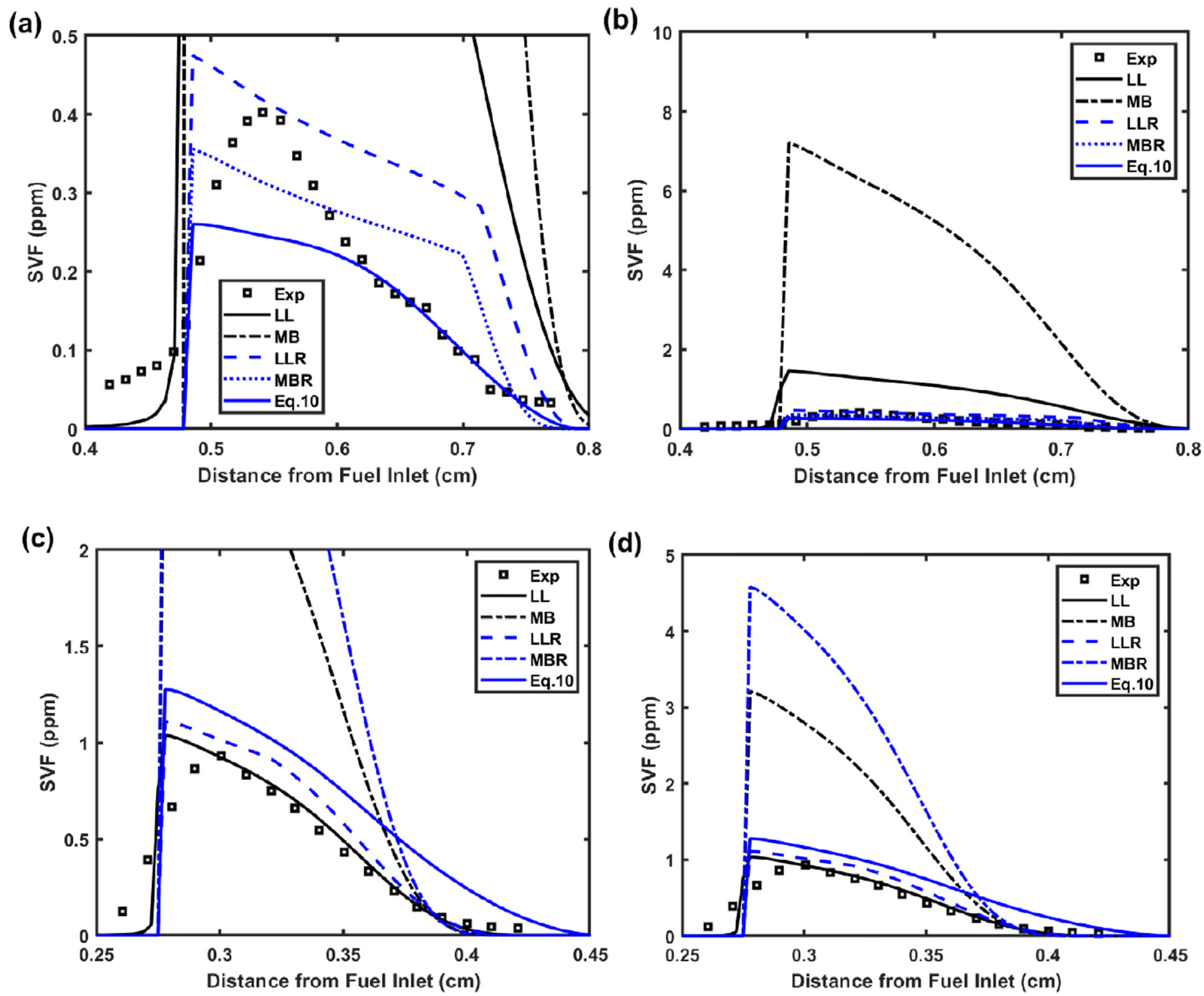

Fig. 9. Predicted *svf* vs. distance from *psp* for all models. a) Hwang SF 0.20 (zoomed in); b) Hwang SF 0.20 (full scale); c) Xu SF 0.30 (zoomed in); d) Xu SF 0.30 (full scale). See Table 1 for flame conditions. (For interpretation of the references to colour in this figure legend, the reader is referred to the web version of this article.)

decreases. At $Z_{st} = 0.393$ (blue), there is no inception. For comparison, the LL inception without reversibility is shown in Fig. 6d.

The results for the MBR model are shown in Fig. 7 and are similar to the LLR model. The rate is more strongly affected (diminishes faster) at elevated Z_{st} due to the greater sensitivity of the surface term (Eq. (15) has $\omega_S \sim A_s$ while Eq. (12) has $\omega_S \sim A_s^{0.5}$). The comparison of this effect between two models has been previously discussed [20].

Figure 8 shows the three reversible models (Eq. (10), LLR, MBR) plus the original models (LL, MB) for three increasing Z_{st} flame conditions, so that the model progression can be observed. While all models show agreeable predictions of *svf* compared to experimental measurements for the low Z_{st} flame (Fig. 8a), only the three reversible models predict soot quantities under the diagnostic limit for the blue flame, while the LL and MB models overpredict (discussed in [20]). The fact that even a one-step model can outperform standard semi-empirical models at this condition by including a single temperature-based reversibility term highlights the importance of accounting for this feature at these conditions. Including reversibility is a necessary and sufficient condition for modeling soot at elevated Z_{st}.

To show the robust nature of these reversible models, predictions from the five models are shown in Fig. 9 for two other counterflow flames where *svf* profiles have been measured. Results comparing predictions against measurements found in Hwang et al. [14] can be seen in Fig. 9a, 9b. This flame has different burner dimensions, inlet velocities (lower strain rate), and flame temperature (2322 K) than the flames listed above (2517 K); full details are in Table 1. For this flame, the original LL model overpredicted the experimental peak *svf* by a factor of 3 (see Fig. 9b) while the LLR model shows good agreement with the experiment. The MB model overpredicted the peak *svf* by over an order of magnitude while the modified MBR model also shows good agreement. The new model presented here Eq. (10)) is close to the experimental measurements, only slightly underpredicting the peak *svf*. Results comparing predictions against measurements from Xu, et al. [24] are shown in Fig. 9c, 9d. The oxygen concentration is enhanced in this flame ($X_{O_2} = 0.30$) such that Z_{st} slightly increases but the flame temperature increases (2649 K) significantly compared to the flame series above. Here, both the LL and LLR give very similar results (see Fig. 9c) and both align well with the experimental *svf*. The MB and MBR models overpredict the experimental *svf* by over a factor of 3 and 4, respectively. The model in Eq. (10) again performs well, with very slight overprediction. It is emphasized that the reversible models required no further adjustment to the fitting constants (e.g. k_{rev} in Eqs. (6,19,20) from the Z_{st} flame series in Table 1). These results indicate that LLR will either maintain the same predictions or will improve them compared to LL. The results for MB and MBR are less conclusive for these flames as neither model performs very well. This is not surprising considering that the LL surface growth constants were fitted in a counterflow flame while MB was fitted for a coflow flame where growth regimes can be different (compare Eqs. (17)-(18) with Eqs. (21)-(22). We therefore assert that the reversibility term proposed here is a robust feature that does not diminish prediction capability in more-traditional non-premixed counterflow flame environments.

These results indicate that the Eq. (10) and LLR models are accurate for a wide range of counterflow flame conditions and that the reversibility framework yields a net modeling improvement, although further research is needed to fully validate these models under alternative flame conditions, flame types, and fuels. Adjustments to empirical constants may be necessary in each case. While these models have been developed through examination of flames of aliphatic fuels only, the deformation of aromatic species that is captured in these models occurs generally in regions of high H atom concentration, regardless of the parent fuel type. The findings in Table 2 suggest that the balance between formation and deformation that occurs at $\Phi = 0.65$ in limit flames could be ubiquitous, and this implies that it is ultimately the ratios of C, H, and O that govern. Therefore, the modeling approach outlined here could be extended to aromatic or oxygenated fuels, provided that a soot inception limit can be observed. However, considering the standard definition of equivalence ratio (ratio between the oxygen content in the oxidant supply and that required for complete stoichiometric combustion) and the derivation of Eq. (2), caution should be exercised when trying to use Eq. (2) to calculate Φ in the case of oxygenated fuels, since this equation only considers oxygen originating from the oxidizer stream.

6. Conclusions

A new approach has been developed for semi-empirical soot models which can capture the changes in soot formation as Z_{st} is modified by accounting for both formation processes as well as important reversibilities which counteract formation. This approach uses a temperature-based term to approximate the chemical reversibilities which counter soot formation. This reversibility term was used alongside an original one-step formation model and was also added as an extension to two existing semi-empirical models (Leung-Lindstedt and Moss-Brookes).

Using this modeling approach resulted in all three models matching experimental measurements at low Z_{st} (25% O_2). More importantly, all three models correctly predicted blue (soot-free) conditions in a non-premixed counterflow flame for the first time. By comparison with models that did not include reversibility, it was demonstrated that this result cannot be obtained by considering formation processes alone. This study, therefore, shows that the performance of semi-empirical soot formation models can be dramatically improved when applied to higher-Z_{st} flames if the reversible nature of soot formation at high temperature is considered.

The models produced in this study showed good agreement with experimental *svf* profiles for sample flames of two other experimental data sets. Results showed that Leung-Lindstedt was either improved or that an accurate status quo was achieved while the Moss-Brookes results were less accurate (with or without the reversibility term). By using a variety of flame conditions, it is shown that while this reversibility framework is simple, it is also robust and applicable for a wide range of counterflow flames. Finally, there is a need for additional experimental measurement of *svf* in higher-Z_{st} flames to validate such models.

Declaration of Competing Interest

The authors declare that they have no known competing financial interests or personal relationships that could have appeared to influence the work reported in this paper.

Acknowledgements

The authors acknowledge partial financial support for carrying out this research from Washington University's Department of Energy, Environmental and Chemical Engineering, and the US National Science Foundation (AGS-1455215 and AGS-1926817).

Supplementary materials

Supplementary material associated with this article can be found, in the online version, at doi:10.1016/j.combustflame.2021.02.029.

References

[1] H. Wang, Formation of nascent soot and other condensed-phase materials in flames, Proc. Combust. Inst. 33 (2011) 41–67.
[2] Y. Wang, A. Raj, S.H. Chung, Soot modeling of counterflow diffusion flames of ethylene-based binary mixture fuels, Combust Flame 162 (2015) 586–596.
[3] C. Saggese, S. Ferrario, J. Camacho, A. Cuoci, A. Frassoldati, E. Ranzi, H. Wang, T. Faravelli, Kinetic modeling of particle size distribution of soot in a premixed burner-stabilized stagnation ethylene flame, Combust Flame 162 (2015) 3356–3369.
[4] J. Appel, H. Bockhorn, M. Frenklach, Kinetic modeling of soot formation with detailed chemistry and physics: laminar premixed flames of C 2 hydrocarbons, Combust Flame 121 (2000) 122–136.
[5] D. Chen, Z. Zainuddin, E. Yapp, J. Akroyd, S. Mosbach, M. Kraft, A fully coupled simulation of PAH and soot growth with a population balance model, Proc. Combust. Inst. 34 (2013) 1827–1835.
[6] V. Chernov, M.J. Thomson, S.B. Dworkin, N.A. Slavinskaya, U. Riedel, Soot formation with C1 and C2 fuels using an improved chemical mechanism for PAH growth, Combust Flame 161 (2014) 592–601.
[7] A. Cuoci, A. Frassoldati, T. Faravelli, E. Ranzi, Formation of soot and nitrogen oxides in unsteady counterflow diffusion flames, Combust Flame 156 (2009) 2010–2022.
[8] M. Sander, R.I. Patterson, A. Braumann, A. Raj, M. Kraft, Developing the PAH-PP soot particle model using process informatics and uncertainty propagation, Proc. Combust. Inst. 33 (2011) 675–683.
[9] A. Fluent, 12.0 Theory Guide, 5, Ansys Inc, 2009.
[10] S.A. Skeen, G. Yablonsky, R.L. Axelbaum, Characteristics of non-premixed oxygen-enhanced combustion: II. Flame structure effects on soot precursor kinetics resulting in soot-free flames, Combust Flame 157 (2010) 1745–1752.
[11] K.O. Johansson, M.P. Head-Gordon, P.E. Schrader, K.R. Wilson, H.A. Michelsen, Resonance-stabilized hydrocarbon-radical chain reactions may explain soot inception and growth, Science 361 (2018) 997–1000.
[12] S.A. Skeen, G. Yablonsky, R.L. Axelbaum, Characteristics of non-premixed oxygen-enhanced combustion: I. The presence of appreciable oxygen at the location of maximum temperature, Combust Flame 156 (2009) 2145–2152.
[13] U. Vandsburger, I. Kennedy, I. Glassman, Sooting counterflow diffusion flames with varying oxygen index, Combust. Sci. Technol. 39 (1984) 263–285.
[14] J. Hwang, S. Chung, Growth of soot particles in counterflow diffusion flames of ethylene, Combust Flame 125 (2001) 752–762.
[15] B. Kumfer, S. Skeen, R. Axelbaum, Soot inception limits in laminar diffusion flames with application to oxy–fuel combustion, Combust Flame 154 (2008) 546–556.
[16] C. Lou, X. Chen, W. Yan, Y. Tian, B. Kumfer, Effect of Stoichiometric Mixture Fraction on Soot Fraction and Emission Spectra with Application to Oxy-Combustion In Progress, (2017).
[17] A. Gopan, Z. Yang, B.M. Kumfer, R.L. Axelbaum, Effects of inert placement (Zst) on soot and radiative heat flux in turbulent diffusion flames, Energy Fuels 31 (2017) 7617–7623.
[18] J. Du, R. Axelbaum, The effect of flame structure on soot-particle inception in diffusion flames, Combust Flame 100 (1995) 367–375.
[19] V.R. Lecoustre, P.B. Sunderland, B.H. Chao, R.L. Axelbaum, Numerical investigation of spherical diffusion flames at their sooting limits, Combust Flame 159 (2012) 194–199.
[20] P.R. Johnson, R.K. Chakrabarty, B.M. Kumfer, Evaluation of semi-empirical soot models for nonpremixed flames with increased stoichiometric mixture fraction and strain, Combust. Flame 219 (2020) 70–85.

[21] R.J. Kee, F.M. Rupley, J.A. Miller, Chemkin-II: A Fortran Chemical Kinetics Package For the Analysis of Gas-Phase Chemical Kinetics, Sandia National Labs., Livermore, CAUSA, 1989.
[22] Y. Wang, S.H. Chung, Effect of strain rate on sooting limits in counterflow diffusion flames of gaseous hydrocarbon fuels: sooting temperature index and sooting sensitivity index, Combust. Flame 161 (2014) 1224–1234.
[23] Y. Wang, S.H. Chung, Strain rate effect on sooting characteristics in laminar counterflow diffusion flames, Combust. Flame 165 (2016) 433–444.
[24] L. Xu, F. Yan, M. Zhou, Y. Wang, S.H. Chung, Experimental and soot modeling studies of ethylene counterflow diffusion flames: non-monotonic influence of the oxidizer composition on soot formation, Combust. Flame 197 (2018) 304–318.
[25] D.X. Du, R.L. Axelbaum, C.K. Law, Experiments on the sooting limits of aerodynamically-strained diffusion flames, Sympo. (International) Combust. 22 (1989) 387–394.
[26] P. Elvati, A. Violi, Thermodynamics of poly-aromatic hydrocarbon clustering and the effects of substituted aliphatic chains, Proc. Combust. Inst. 34 (2013) 1837–1843.
[27] N.A. Eaves, S.B. Dworkin, M.J. Thomson, The importance of reversibility in modeling soot nucleation and condensation processes, Proc. Combust. Inst. 35 (2015) 1787–1794.
[28] B. Chao, S. Liu, R. Axelbaum, On soot inception in nonpremixed flames and the effects of flame structure, Combust. Sci. Technol. 138 (1998) 105–135.
[29] Y. Wang, S.H. Chung, Soot formation in laminar counterflow flames, Prog Energy Combust Sci 74 (2019) 152–238.
[30] B. Kumfer, S. Skeen, R. Chen, R. Axelbaum, Measurement and analysis of soot inception limits of oxygen-enriched coflow flames, Combust Flame 147 (2006) 233–242.
[31] D.X. Du, R.L. Axelbaum, C.K. Law, Soot formation in strained diffusion flames with gaseous additives, Combust. Flame 102 (1995) 11–20.
[32] K.M. Leung, R.P. Lindstedt, W.P. Jones, A simplified reaction mechanism for soot formation in nonpremixed flames, Combust. Flame 87 (1991) 289–305.
[33] S.J. Brookes, J.B. Moss, Predictions of soot and thermal radiation properties in confined turbulent jet diffusion flames, Combust. Flame 116 (1999) 486–503.